High-Performance Metal Oxide Nanoparticle Materials Synthesised Using Polar Aprotic Solvents for Advanced Supercapacitor Applications.

Authors: Muhammad Nasir Hussain[a,b], Abid Inayat[a], Syed Mujtaba Shah[a], Mohammad Ihsun[b], Ali Haider[a], Syed Mustansar Abbas[c], Stephen G. Hickey[b*]

a. *Department of Chemistry, Quaid-i-Azam University, Islamabad, 45320, Pakistan.*
b. *School of Chemistry and Biosciences, University of Bradford, BD7 1DP, United Kingdom.*
c. *Nanoscience and Technology Department, National Centre for Physics, Islamabad, Pakistan.*

Physical Characterization and Sample Preparation Methods

Powder X-ray Diffraction (XRD).

P-XRD analysis was recorded on a Bruker advance AXS D8 diffractometer using a Cu source running at 30 kV and 10 mA with the as-prepared nanostructured powders being placed on a silicon wafer. The instrument was controlled using the WinXPow software package and the materials were referenced using the inorganic Crystal Structure Database.

Raman and FT-IR Spectroscopy.

Raman spectra of the as-prepared nanostructures were obtained following excitation using a 633 nm diode-pumped solid-state laser and recorded on a Renishaw InVia instrument equipped with a Leica microscope at a spectral resolution of approximately 2 cm^{-1}. The samples were prepared by spreading the nanostructured powder onto a thin Al film. To prevent samples from heating under the microscope lens, the incident laser power was maintained below 0.02 mW. Furthermore, additional information concerning the chemical nature of the nanostructures was elucidated via FT-IR (PerkinElmer Frontier 100) equipped with attenuated total reflectance (ATR), with the IR beam directed onto the sample from below to a depth of 1 to 2 micrometres.

X-ray photoelectron spectroscopy (XPS).

A Kratos Axis Super XPS (X-ray Photoelectron Spectroscopy) instrument equipped with a monochromatic Al K_α X-ray source ($h\upsilon$ = 1486.6 eV) was used to carry out XPS analysis. The adventitious C 1s peak, with a binding energy of 284.8 eV, was taken as reference against which the binding energies of all other elements are quoted.

Scanning electron microscopy, elemental mapping, and energy-dispersive X-ray spectroscopy.

SEM was used to analyse the surface morphology of the as-prepared nanostructures. The scanning electron microscope (SEM, FEI Quanta 400) was equipped with an Oxford Instruments Xplore 30 EDS detector. The samples were prepared by uniformly depositing powders on Al stubs followed by sputtering with a layer of carbon to prevent the build-up of charge. Furthermore, elemental mapping and energy-dispersive X-ray spectroscopy (EDX) were carried out simultaneously using conventional SEM analysis to determine the homogeneous particle distribution and composition. The images were recorded using an accelerating voltage of 10 kV and the spectra were acquired for 300 s live time. Standardless quantification was applied using Aztec Energy EDS software.

Transmission Electron Microscopy (TEM).

Transmission electron microscopy images of the as-prepared samples were acquired by dispersion of the samples in water, dropping onto carbon coated copper grids followed by solvent evaporation. Imaging was carried out on a JEOL JEM-1200 EX MKII microscope, equipped with a thermionic gun (tungsten filament), operating at an acceleration voltage of 120 kV.

Thermogravimetric analysis (TGA) and differential scanning calorimetry (DSC).

TGA profiles of as-prepared nanostructures were measured using a TA Instruments Q5000, under inert atmosphere (N_2) and a heating rate of 10 K min^{-1}. DSC analysis was carried out under the same conditions using a TA Instruments Q2000. The TA universal analysis software suite was employed to evaluate the data in both cases.

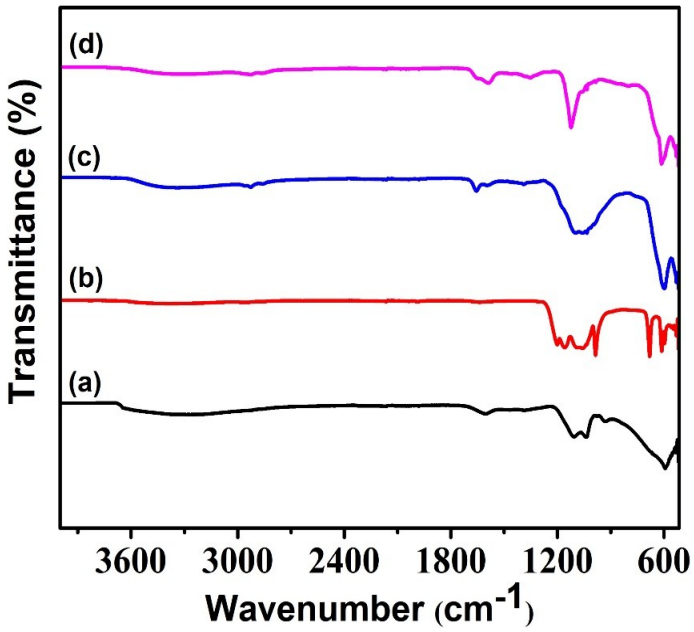

Fig. S1. *FT-IR spectra of nanostructures (a) α-$Ni(OH)_2$ nanoparticles, (b) NiO nanoparticles, (c) MnO_2 nanosheets, (d) α-$Ni(OH)_2$–MnO_2 hybrid nanomaterial.*

FTIR spectra of the as-prepared nanostructures are presented in **Fig. S1**. The strong absorption peak at 590 cm^{-1}, (**Fig. S1(a)**) can be ascribed to the Ni-OH stretching vibration modes of α-$Ni(OH)_2$. The broad band at 3360 cm^{-1} is assigned to the vibration of O-H groups and is due to the retention of small quantities of adsorbed water by the α-$Ni(OH)_2$ nanoparticles. The sharp peak around 1610 cm^{-1} is characteristic of the bending mode of adsorbed water molecules. The appearance of the signal at 1031 cm^{-1} confirms the

existence of carbonate ions which may be due to the adsorption of atmospheric CO_2 by the hydroxide sample either during the analysis or the drying of the sample. The peaks observed at 610 cm^{-1} and 685 cm^{-1} in the FTIR spectrum of NiO nanoparticles **Fig. S1(b)**, correspond to the stretching mode of the Ni-O bond. It can also be seen from the profile that the broad O-H vibrations at 3360 cm^{-1} have disappeared due to the dehydroxylation of α-$Ni(OH)_2$ into NiO when thermally decomposition occurs at 500°C. The peaks that appear at 986 cm^{-1} and 1150 cm^{-1} can be ascribed to the stretching vibrational modes of C-O and SO_4 groups. Additionally, the FT-IR spectra of MnO_2 and α-$Ni(OH)_2$-MnO_2 hybrid nanostructures display peaks at 3360 cm^{-1}, 1660 cm^{-1} and 1590 cm^{-1} corresponding to the O-H and H-O-H vibrational modes while the peak at 2937 cm^{-1} is due to C-H stretching modes seen in **Fig. S1(c, d)**. The peaks at 1090 cm^{-1} and 1125 cm^{-1} are ascribed to the O-H bending modes. The absorption band at 598 cm^{-1} is characteristic of O-Mn-O stretching. Moreover, the vibrational atomic modes of the α-$Ni(OH)_2$-MnO_2 nanostructure were confirmed by the presence of two strong bands at 613 cm^{-1}, corresponding to Ni-O or O-Mn-O stretching **(Fig. S1(d))**.

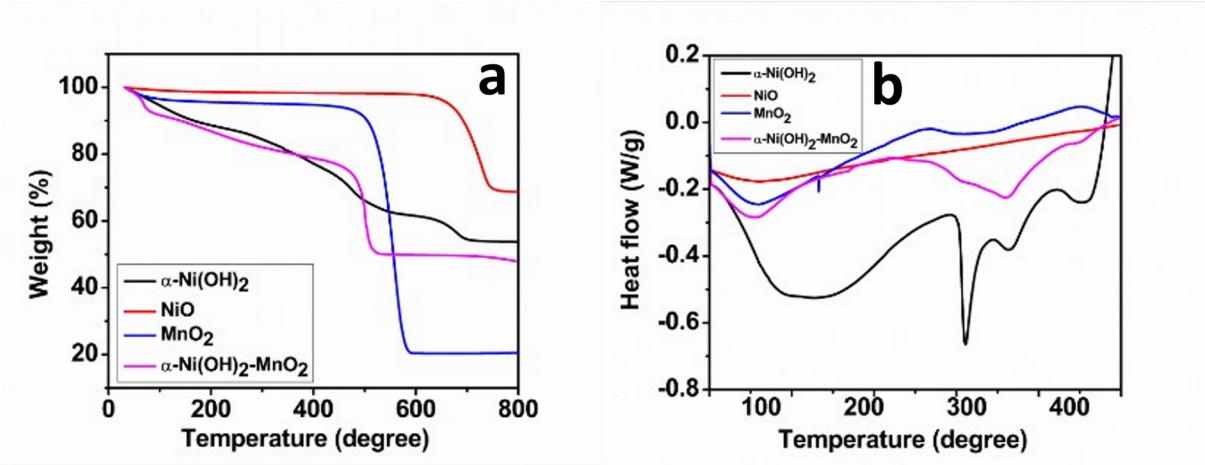

Fig. S2. *(a) TGA and (b) DSC profiles of the nanomaterials measured under an N_2 atmosphere with a heating rate of 10 K min^{-1}.*

The thermal changes that occur during the heat treatment between 20 and 800 °C of the as-prepared nanostructures are presented in Figure S2. TGA analysis, **Fig. S2(a)** of the α-$Ni(OH)_2$ nanoparticles exhibit three principal mass loss steps; a mass loss of approx. 13% occurs from 20 to 250 °C which is due to the evaporation of water of crystallisation, a mass loss of approximately 24% from 260 to 550 °C, which represents the elimination of water molecules associated with the thermal decomposition of α-$Ni(OH)_2$ to NiO nanoparticles[1] and a mass loss of approx. 6% in the region from 630 to 700 °C due to the oxidation of carbon to CO_2. The TGA profile of the NiO nanoparticles shows a continuous mass loss of approx. 27.6% in the temperature range from 630 to 750 °C which can be assigned to the oxidation of carbon, present as

organic material, to CO_2. At temperatures higher than 750 °C the TGA curve remains constant, which indicates that all carbon present has been converted to CO_2. Two mass loss events were detected for MnO_2 nanoparticles with the first, occurring under 100 °C and accounting for approx. 4% loss, is due to traces of moisture bound at the particle surface. and the second occurring from 500 to 600 °C and is most likely associated with the phase transformation of two MnO_2 units to form Mn_2O_3. For the α-$Ni(OH)_2$–MnO_2 hybrid nanostructures, the mass loss of approx. 8% that occurs under 100 °C corresponds to the evaporation of surface adsorbed water, the mass loss of approx. 16% that occurs between 110 and 440 °C can be ascribed to the conversion of α-$Ni(OH)_2$ to NiO and the mass loss of approx. 26% that occurs from 480 to 530 °C is related to transformation of MnO_2 to Mn_2O_3.

The DSC profiles confirm the TGA observations and are presented in **Fig. S2(b)**. α-$Ni(OH)_2$ nanoparticles display a broad peak in the region below 200°C which is related to the energy required to bring about the evaporation of strongly adsorbed water from the surface. In addition, α-$Ni(OH)_2$ exhibits a sharp and intense endothermic peak at 300°C with two, less intense peaks at 340 °C and 415 °C. The temperature range of these endothermic peaks matches well with that of the mass loss corresponding to the decomposition of α-$Ni(OH)_2$ to form NiO. NiO nanoparticles do not show any observable thermal behaviour in their DSC profiles, which is to be expected as NiO is obtained by the high temperature decomposition of α-$Ni(OH)_2$ at 500°C. For MnO_2 and α-$Ni(OH)_2$–MnO_2 two endothermic peaks can be observed in each of the DSC profiles when the temperature is increased from 50 °C to 450 °C. The lower temperature endothermic peak below 100 °C is related to the loss of absorbed water molecules incorporated during the synthesis. The broad band observed in the region from 300 °C to 340 °C is due to mass losses associated with the structurally associated water molecules.

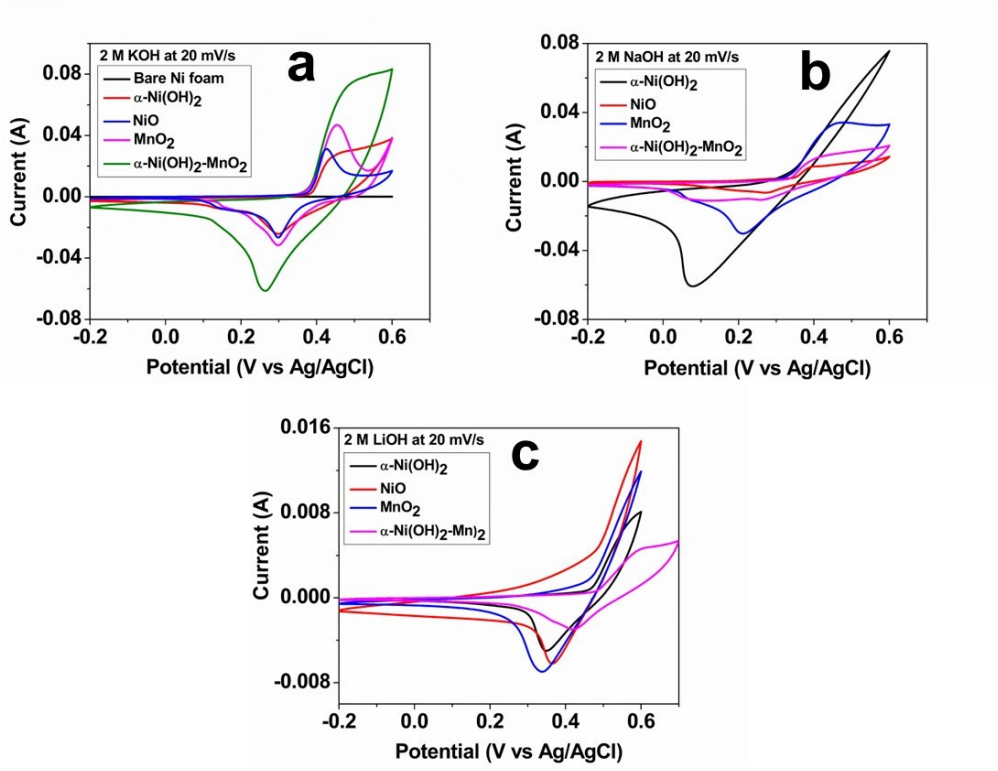

Fig. S3. *CV profiles of α-Ni(OH)$_2$, NiO, MnO$_2$, and α-Ni(OH)$_2$–MnO$_2$ hybrid in (a) KOH, (b) NaOH, and (c) LiOH.*

Electrochemical Measurements in Aqueous Electrolytes.

The electrochemical behaviour of all four nanomaterials in various aqueous electrolytes, such as KOH, NaOH and LiOH, have been investigated. The CV profiles of each material, along with that of the bare nickel foam, recorded within the potential window of -0.2 to 0.6 V and at a scan rate of 20 mV/s in 3 M KOH, NaOH, and LiOH are presented in **Fig. S3(a, b, c)**. It is found that the area encompassed by the bare nickel foam curve **(a)** is negligible, demonstrating a significantly smaller charge storage capacity than the active materials. In contrast, the area enclosed within the CV curves increases in the different electrolytes in the order LiOH < NaOH < KOH, indicating a good electrochemical performance of the synthesized materials. Of the three electrolytes employed here, the active materials display a clearly defined pair of redox peaks in KOH indicating its suitability for further electrochemical studies. The trends in the electrochemical performance observed can be explained by the hydrated ionic radii of the electrolyte cations with K^+ (0.3 nm) possessing the smallest of the three hydrated ionic radii compared to Na^+ (0.4 nm) and Li^+ (0.6 nm).[2]

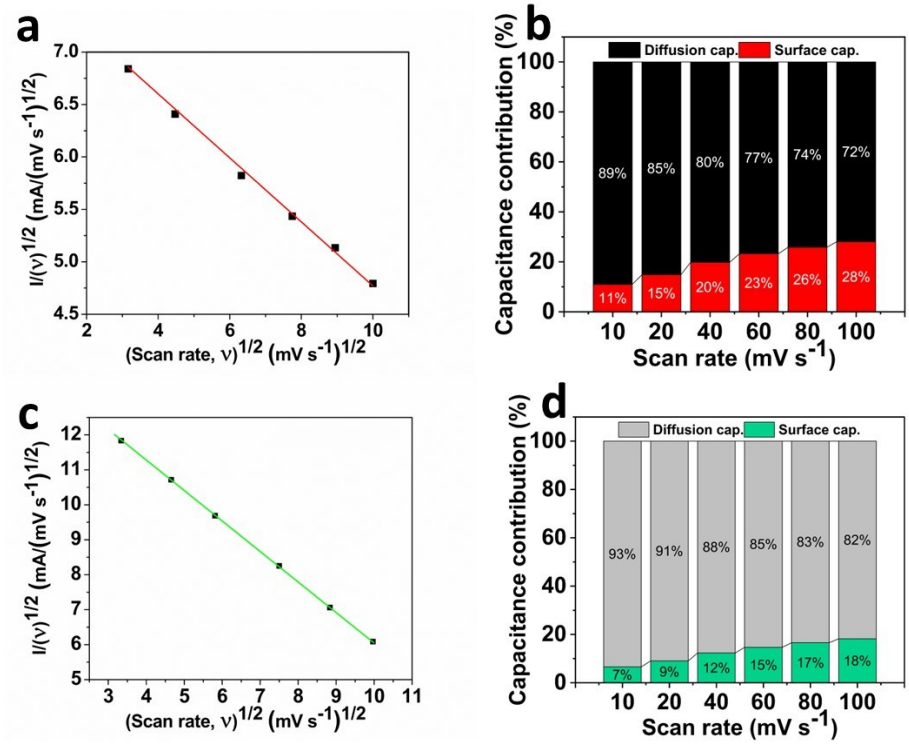

Fig.S4. *Quantitative capacitive analysis of α-Ni(OH)$_2$ and MnO$_2$ hybrid material, (a, c) plots of ($i/v^{1/2}$) vs ($v^{1/2}$), (b, d) contribution of surface and diffusion capacities at various scan rates.*

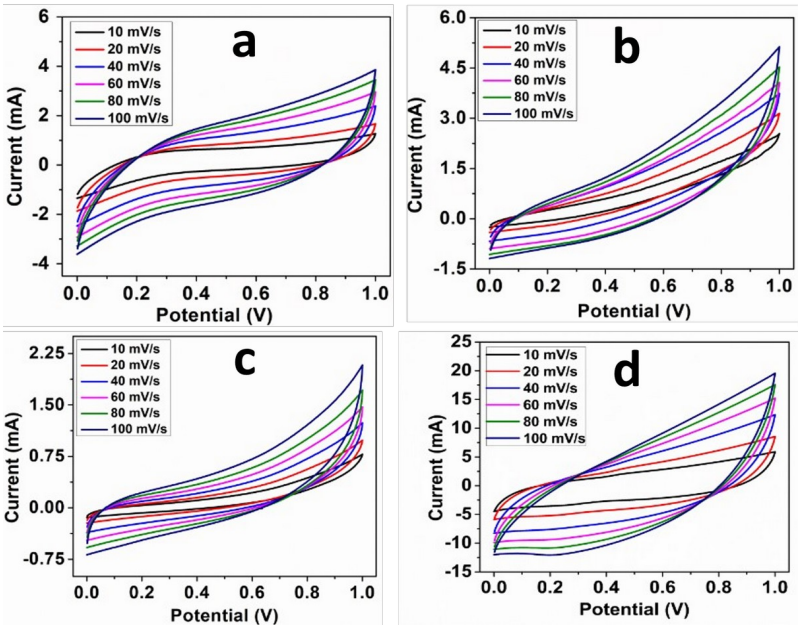

Fig. S5. CV profiles of symmetric devices of a) α-Ni(OH)$_2$ nanoparticles, b) NiO nanoparticles, c) MnO$_2$ nanoparticles and d) α-Ni(OH)$_2$–MnO$_2$ hybrid.

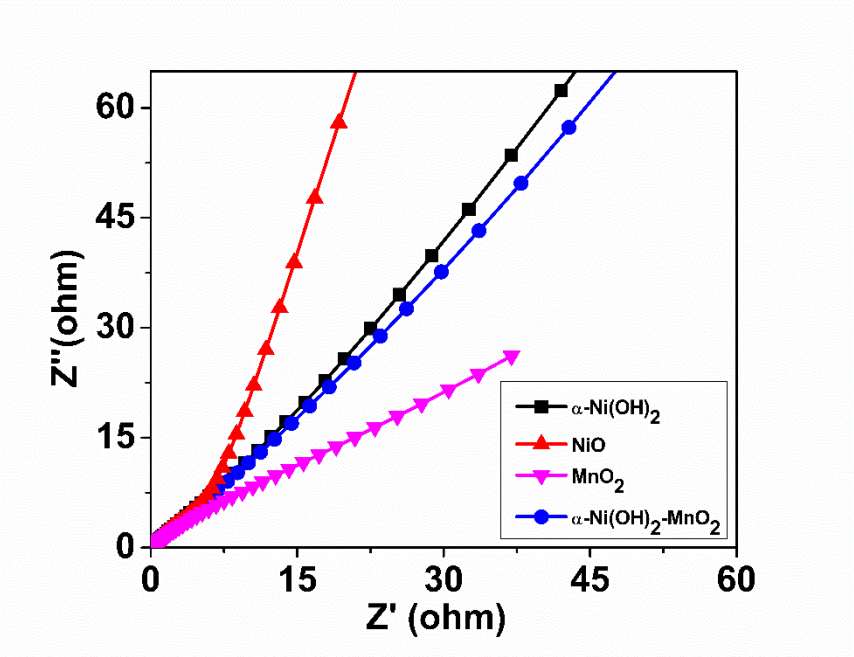

Fig. S6. *Nyquist plots after cyclic stability test.*

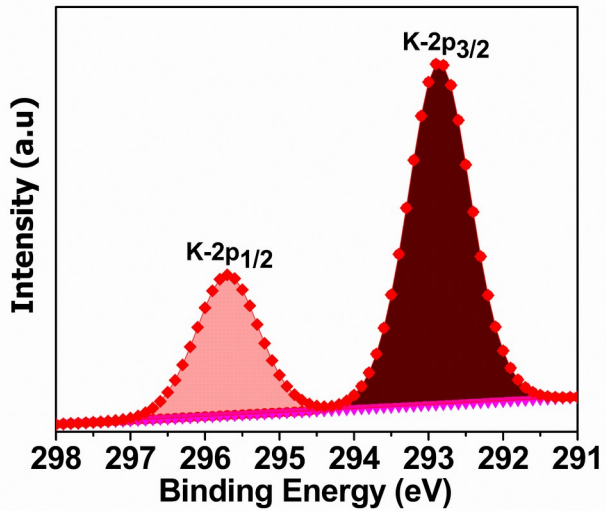

Fig. S7. *XPS profile of k-2p which appeared after the stability test.*

The k-2p peaks appear in the XPS spectra due to the presence of KOH which was employed as the background electrolyte for the electrochemical investigations. The before and after XPS spectrum confirms that no oxidation state changes occurred for each element present in the α-$Ni(OH)_2$ and MnO_2 in the hybrid material.

$Ni(OH)_2$ Crystallite size.

Sr. No	K	Wavelength	2-Theta	FWHM	Crystallite Size
1	0.94	1.54178	11.78542	3.23025	2.58427
2	0.94	1.54178	24.12559	3.46917	2.44762
3	0.94	1.54178	34.00855	4.60474	1.88574
4	0.94	1.54178	60.13117	3.42287	2.8031

NiO Crystallite size.

Sr. No	K	Wavelength	2-Theta	FWHM	Crystallite Size
1	0.94	1.54178	37.39479	1.06238	8.25163
2	0.94	1.54178	43.49531	1.24824	7.16211
3	0.94	1.54178	63.13925	1.42509	6.83894
4	0.94	1.54178	75.71695	1.70905	6.15389

MnO_2 Crystallite size.

Sr. No	K	Wavelength	2-Theta	FWHM	Crystallite Size
1	0.94	1.54178	18.40761	0.37355	22.51914
2	0.94	1.54178	29.38925	0.50559	16.97919
3	0.94	1.54178	32.99512	0.75573	11.45945
4	0.94	1.54178	36.39979	0.42851	20.39862
5	0.94	1.54178	44.69062	0.42249	21.24992
6	0.94	1.54178	60.44018	0.80971	11.86807

α-$Ni(OH)_2$-MnO_2 Crystallite Size.

Sr. No	K	Wavelength	2-Theta	FWHM	Crystallite Size
1	0.94	1.54178	18.35605	0.36204	23.23337
2	0.94	1.54178	31.13158	0.58201	14.81053
3	0.94	1.54178	33.07908	0.67515	12.82994
4	0.94	1.54178	36.28721	0.55359	15.7846
5	0.94	1.54178	60.51974	0.81743	11.76075

The particle sizes reported above have been obtained from PXRD are thus derived indirectly from the width of diffraction peaks in the X-ray diffraction pattern. The size information provided by PXRD is therefore that of the crystallite domain sizes within the material but does not necessarily represent the actual spatial particle size as PXRD assumes ideal crystal geometry and neglects the presence of non-crystalline components, defects, and other surface effects. TEM images directly provide the spatial extent of individual particles at the nanoscale and so provides a representation of the particles that includes their morphology, size, and size distribution. Consequently, it is not uncommon for these two techniques to differ in the particle sizes they report.

References

[1] M. El-Kemary, N. Nagy, I. El-Mehasseb, *Mater. Sci. Semicond. Process.* **2013**, *16*, 1747-1752.

[2] R. Deka, R. Rajak, V. Kumar, S. M. Mobin, *Inorg. Chem.* **2023**, *62*, 3084–3094.